NANOMATERIALS

Toughness of carbon nanotubes conforms to classic fracture mechanics

10.1126/sciadv.1500969

Lin Yang,* Israel Greenfeld,*† H. Daniel Wagner†

Defects in crystalline structure are commonly believed to degrade the ideal strength of carbon nanotubes. However, the fracture mechanisms induced by such defects, as well as the validity of solid mechanics theories at the nanoscale, are still under debate. We show that the fracture toughness of single-walled nanotubes (SWNTs) conforms to the classic theory of fracture mechanics, even for the smallest possible vacancy defect (~2 Å). By simulating tension of SWNTs containing common types of defects, we demonstrate how stress concentration at the defect boundary leads to brittle (unstable) fracturing at a relatively low strain, degrading the ideal strength of SWNTs by up to 60%. We find that, owing to the SWNT's truss-like structure, defects at this scale are not sharp and stress concentrations are finite and low. Moreover, stress concentration, a geometric property at the macroscale, is interrelated with the SWNT fracture toughness, a material property. The resulting SWNT fracture toughness is 2.7 MPa $m^{0.5}$, typical of moderately brittle materials and applicable also to graphene.

INTRODUCTION

Theoretical studies predict that the strength of carbon nanotubes (CNTs) should be of the order of 200 GPa, owing to their strong sp^2 carbon-carbon bonds and hexagonal network structure. This high strength is well matched with the CNTs' outstanding Young's modulus of about 1 TPa (*1*–*3*) and their high ultimate strain of 20% (*4*–*6*). Although the theoretical value of Young's modulus is well substantiated experimentally (*1*, *3*), measured strength values are lower than predicted, in the range of 11 to 120 GPa (*7*–*11*) at maximum strain of 2 to 13%, and are widely dispersed statistically (*9*). It is generally accepted that these discrepancies in strength and strain are the consequence of the presence of topological and point defects in the CNT crystalline structure (*12*–*15*), commonly induced during CNT growth, purification, dispersion, chemical treatment, and irradiation (*12*).

Although CNT fracturing at high temperatures was theoretically shown to be of a plastic nature (*2*), it is still debated whether the fracture mechanism at room temperature is plastic or brittle. Plastic deformation, characterized by the appearance and spreading of topological defects via bond breaking and reforming (*16*–*21*), can theoretically occur at room temperature at very high strains (>20%). However, scanning electron microscopy and transmission electron microscopy evidence shows that fracture surfaces of broken CNTs are typically sharp and flat, which is a strong indication that CNTs break in a brittle manner at room temperature (*22*–*26*). Here, we use molecular dynamics (MD) with a maximum allowed bond force criterion to investigate the process and mechanism by which a defect in a single-walled nanotube (SWNT) evolves into a crack that propagates until complete failure. By mapping the stress field around defects of various shapes and sizes, embedded in tubes having different chiralities, we show how local stress concentrations lead to a brittle fracture, thus degrading the ideal strength of SWNTs.

We also address the debate on whether solid mechanics theories apply at the nanoscale, specifically whether a limit size exists below which macroscale theories fail to predict the behavior of nanomaterials [for example, Zhang *et al.* (*14*) found a limit of 10 lattice spacings]. Experimental evaluation of the harm caused by different defect types is not practical [see, for example, the discussion by Barber *et al.* (*8*)]. Hence, we use the wide variety of defect types and sizes simulated in the present study to examine the applicability of concepts from the theories of elasticity and fracture mechanics to the nanoscale crystalline structures of CNTs.

Department of Materials and Interfaces, Weizmann Institute of Science, Rehovot 76100, Israel.
*These authors contributed equally to this work.
†Corresponding author. E-mail: green_is@netvision.net.il (I.G.); daniel.wagner@weizmann.ac.il (H.D.W.)

RESULTS

Stress distribution around atomic defects is nonuniform

A variety of Stone-Wales and vacancy defects (*12*, *13*, *15*) were embedded in SWNT models with armchair and zigzag chiralities, and tension was simulated by applying a constant displacement rate to the SWNT free end (Fig. 1, Materials and Methods, and notes S1 to S4). Stone-Wales—a topological defect—was simulated by rearranging atoms and bonds in the CNT structure, whereas vacancy—a point defect—was simulated by removing atoms from the structure. Bond stresses were continuously monitored, and bond breakage was determined when a maximum allowed bond force of 10 nN was exceeded (*27*, *28*). The simulation model was validated by tensile loading of defect-free tubes, yielding a Young's modulus of 1 TPa for a zigzag tube and 0.88 TPa for an armchair tube, in agreement with the literature (*1*–*3*) (Fig. 2A and note S3). The stresses were uniformly distributed throughout the simulated SWNT. The corresponding tensile strengths were about 175 and 200 GPa for the armchair and zigzag tubes, respectively, assuming that the maximum tensile strain of a defect-free SWNT is 20% as predicted theoretically (*4*–*6*).

When a defect is present in an SWNT subjected to tension, stresses are no longer distributed evenly, and stress concentrations arise at the defect tips. The maximum stress concentration factors $K_t = \sigma_{max}/\sigma_{ff}$ (σ_{ff} is the far-field stress and σ_{max} is the maximum stress, defined in Fig. 1A) in SWNTs with vacancy defects are found to vary between 1.2 and 2.7 (Fig. 2B). It is seen that K_t is lowest for monovacancies and is higher for longer defects oriented perpendicularly to the straining axis. Unevenly distributed tensile stresses are observed in an armchair SWNT containing a two-atom vacancy (Fig. 3A) with a high maximum stress occurring at the defect tips (red atoms).

The stress across the defect gap in the axial direction is much lower than the far-field stress (green atoms). The stress concentration factors remain practically constant with the applied strain, as seen, for example, in the case of a two-atom vacancy defect [Fig. 1B(c)] where K_t has values of 1.96, 1.91, and 1.85 for strains of 3, 5, and 10%, respectively.

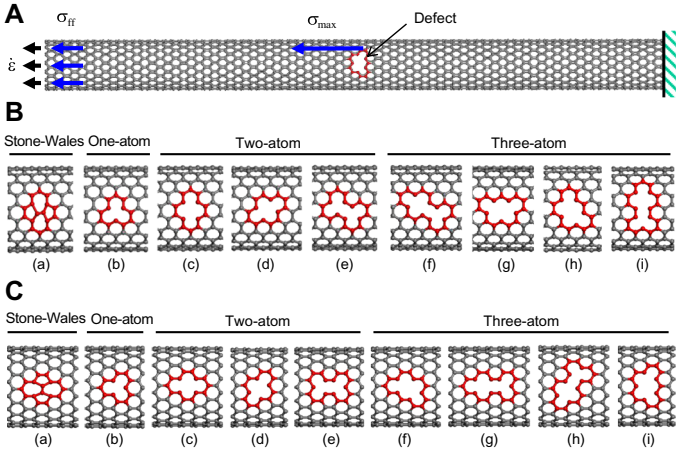

Fig. 1. Simulation models of SWNTs with embedded defects. (**A**) Definition of the simulation protocol for a defective SWNT (length, 170 Å) under axial tension: a constant strain rate $\dot{\varepsilon}$ is applied at the CNT free end, with resulting far-field stress σ_{ff} and maximum stress σ_{max}. (**B**) Simulation models of armchair SWNTs [(10, 10) chirality] with Stone-Wales (a) and vacancy (b to i) defects. The number of missing atoms in vacancies is indicated. (**C**) Simulation models of zigzag SWNTs [(17, 0) chirality] with Stone-Wales (a) and vacancy (b to i) defects.

Propagation of damage is spontaneous and continuous

When the applied strain is increased, the most highly stressed bonds eventually break and the SWNT fractures. In agreement with experimental evidence (*7*–*11*), simulations show that the SWNT strength σ_f is as low as 70 GPa, which is a reduction of about 60% with respect to the ideal strength σ^* of a defect-free SWNT (Fig. 2C). It is seen from the trends of Fig. 2 (B and C) that the relative strength σ_f/σ^* is inversely correlated with K_t and that CNTs with monovacancies are stronger (~20% reduction) than those containing longer defects. The simulations also show that the SWNT strength is not degraded by the presence of multiple vacancy defects, unless several such defects are located at the same longitudinal position.

In the case of Stone-Wales defects, the SWNT strength is determined by a superposition of prestresses, induced by atomic rearrangement, and stress concentration due to nonuniform atomic load sharing (note S5). The prestresses are caused by extension and contraction of bonds, producing respective tension and compression forces. When the tension prestresses coalign with the load, as in a zigzag SWNT, the strength is reduced by almost 40%, whereas when they are perpendicular to the load, as in an armchair SWNT, they only have a slight impact (Fig. 2C and fig. S1).

Crack propagation in an SWNT was simulated by deleting overstressed carbon-carbon bonds without reforming new bonds, while keeping the applied strain constant after first breakage of a bond. The SWNTs begin to rupture at strains as low as 7%, much lower than the 20% of a defect-free SWNT. In all the studied defects, once the first bond is dissociated, the crack propagates spontaneously and continuously until the SWNT fractures, which is a signature of a brittle fracture mechanism. The resulting tensile strength of the simulated structures is the far-field stress at the instant of crack initiation. The example in Fig. 3 (B and C) and movie S1 depicts the fracture process in an SWNT containing a two-atom vacancy defect. As seen, the crack

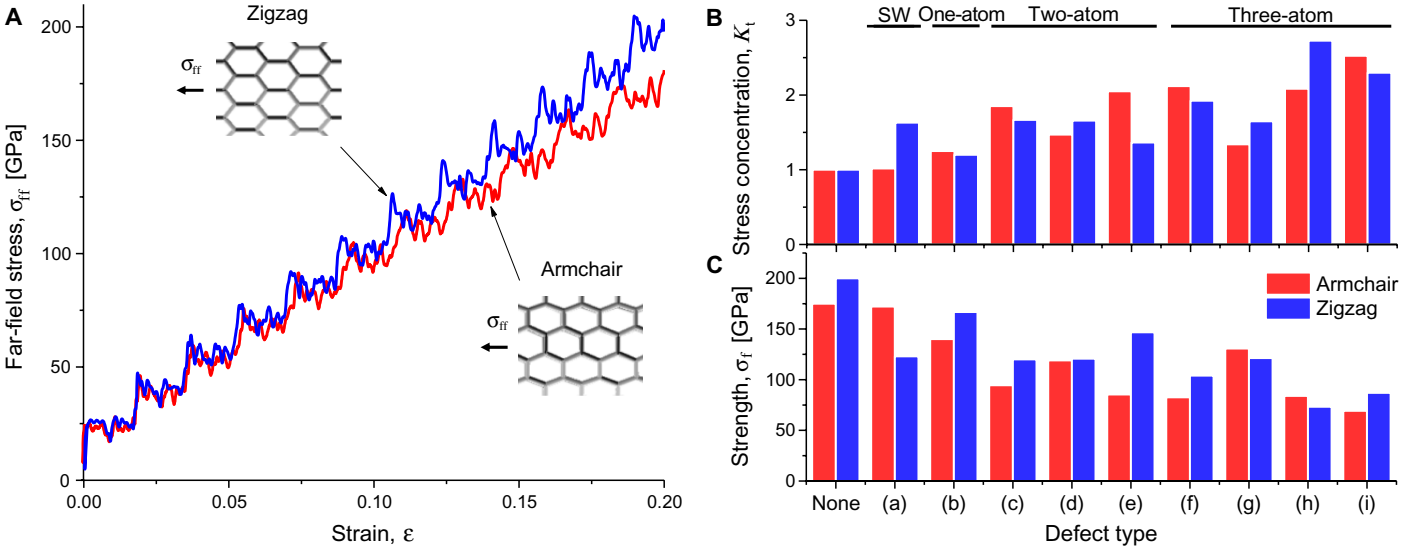

Fig. 2. Simulated stress and strength of SWNTs under tension. (**A**) Stress-strain curves of defect-free zigzag and armchair SWNTs. The images show the SWNTs' deformation at 20% strain. (**B**) Maximum stress concentration K_t in armchair and zigzag SWNTs containing defects of various shapes and sizes (Fig. 1, B and C), at a strain of ~10%. The number of missing atoms in vacancies is indicated at the top of the figure. (**C**) Ultimate tensile strength σ_f in armchair and zigzag SWNTs containing defects of various shapes and sizes. K_t and σ_f data are provided in note S4.

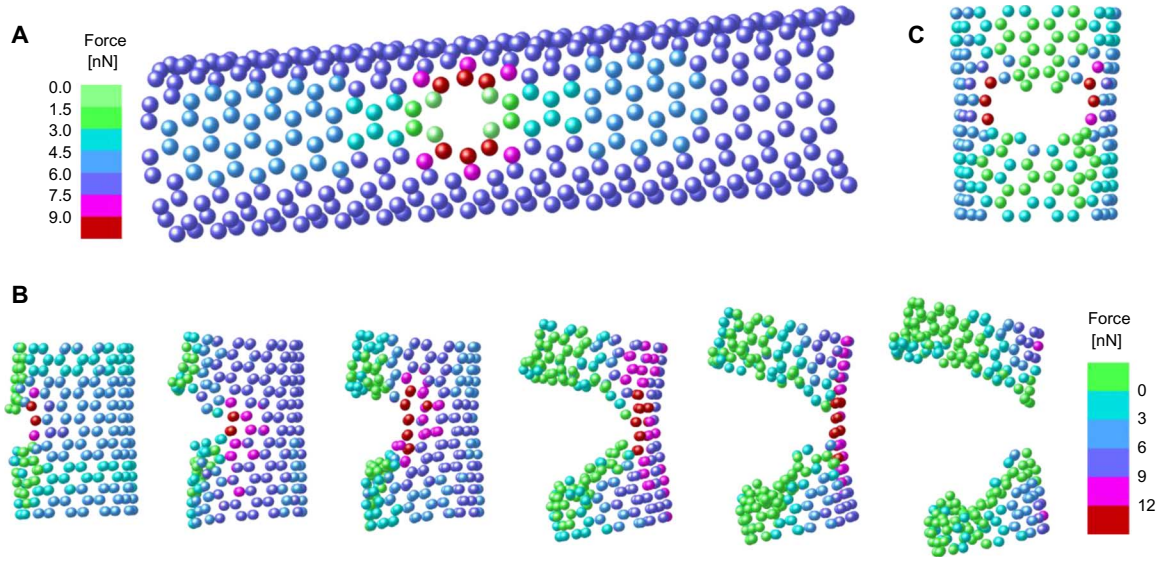

Fig. 3. High stresses around a defect lead to crack propagation. (**A**) Nonuniform stress distribution in an armchair SWNT containing a two-atom vacancy defect [Fig. 1B(c)], under tensile loading at 10% strain, expressed in terms of atom forces in the loading direction. The highest stressed atoms are colored red. (**B**) Spontaneous crack propagation at a fixed strain of 11%. The loading direction is vertical, and the crack is viewed from the side. (**C**) Atom forces around a crack (front view).

propagates in the circumferential direction from both sides of the defect and is driven by the high stress concentrations at the crack tips (red atoms).

Defects in SWNTs cannot be described by elliptical holes

A vacancy defect in a CNT is sometimes considered analogous to an elliptical hole in a thin plate. The stress concentration predicted by linear elasticity for an elliptical hole of semilength a and tip radius ρ, embedded in an infinite-width thin plate, is (*29*)

$$K_t^{LE} = 1 + 2\sqrt{\frac{a}{\rho}} \quad (1)$$

This model provides a good estimate for a wide variety of holes, such as rounded-tip slits, which have the same tip curvature as an equivalent elliptical hole (*29*). The infinite-width plate approximation is elaborated in Materials and Methods.

By contrast, and somewhat unexpectedly, the simulated K_t is found to be predominantly dependent on the defect length $2a$ perpendicular to the tube axis, whereas the effects of defect shape (for example, the ratio a/b) and orientation are found to be insignificant (Fig. 4A and note S6). For example, the number of missing atoms in a defect is not significant, except when they are aligned in a way that increases its length $2a$ (for example, the three-atom vacancies in Fig. 4A). Thus, K_t is compared with K_t^{LE} and depicted against a, normalized by the constant bond length r_0, using a fixed tip radius of $\rho = r_0$ and $\rho = 2r_0$ (green dashed lines in Fig. 4A). It is important to realize that the defect dimensions (length $2a$ and width $2b$) are defined between cell centers, as shown in the drawings in Figs. 4A and 5B and note S4, and not between defect edges or vertices. In this way, when the defect length and width are zero, the shape reverts to a regular hexagonal cell, as expected when no defect is present.

We find that the simulated K_t values are significantly lower than the theoretical values (Eq. 1) for an elliptical hole (Fig. 4A), and hence, SWNTs appear to be less sensitive to stress concentration due to defects than solid materials. That is, the model in Eq. 1 does not fit the simulation results well, even when a large tip radius is assumed ($\rho = 2r_0$ in Fig. 4A). Furthermore, the SWNTs are sensitive to the defect length $2a$ rather than to its shape, in sharp contrast to linear elasticity in which K_t does not depend on size but on the self-similar shape (for example, the ratio a/ρ in Eq. 1). A tighter K_t fit can be achieved by a power expression (red solid line in Fig. 4A), clarified later.

Toughness at the nanoscale conforms to classic fracture mechanics

The strength predicted by linear elastic fracture mechanics (LEFM) (*30*–*32*) for a sharp brittle crack of semilength a in an infinite-width thin plate (plane stress) is given by

$$\sigma_f^{LEFM} = \frac{K_{Ic}}{\sqrt{\pi a}}, \quad K_{Ic} = \sqrt{2E\gamma} \quad (2)$$

where K_{Ic} is the mode I fracture toughness, E is the plate elastic modulus, and γ is the energy required to create two new crack surfaces. The infinite-width plate approximation is elaborated in Materials and Methods.

The simulated relative strength σ_f/σ^* is depicted against the normalized defect length a/r_0 (Fig. 4B) and fits the classic LEFM model of Eq. 2 (the red solid line) well. The fit yields an average fracture toughness of $K_{Ic} = 2.7 \pm 0.3$ MPa $m^{0.5}$ (2.5 ± 0.1 MPa $m^{0.5}$ for the armchair tube and 2.9 ± 0.3 MPa $m^{0.5}$ for the zigzag tube), in ballpark agreement with a recent study on graphene (*33*). An estimate using the expression $K_{Ic} = \sqrt{2E\gamma}$ from Eq. 2 provides similar values (note S7). Using Ashby's material selection guide (*34*), the resulting SWNT K_{Ic} is found to be typical of moderately brittle materials. Its value resides in the high-end range of ceramics (0.2 to 5 MPa $m^{0.5}$) and polymers (0.4 to 4 MPa $m^{0.5}$) and is lower than the K_{Ic} values of metals and alloys (5 to 200 MPa $m^{0.5}$). It is higher than the K_{Ic} values of glass

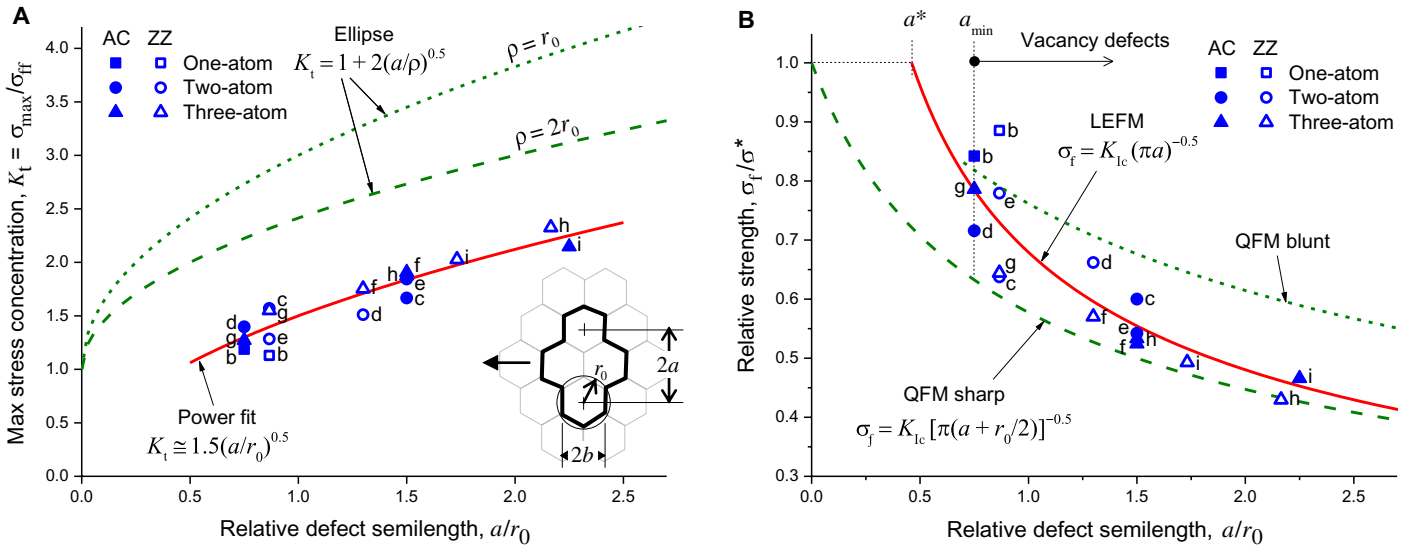

Fig. 4. Comparison of simulation with solid mechanics theories. (**A**) Simulated SWNT maximum stress concentration factor $K_t = \sigma_{max}/\sigma_{ff}$ at ~10% elongation versus the relative defect semilength a/r_0, compared with linear elasticity predictions for an infinite-width thin plate having an elliptical hole with fixed tip radius ($\rho = r_0$ and $\rho = 2r_0$). $r_0 \cong 1.42$ Å is the C═C bond length. The SWNTs have one-atom, two-atom, and three-atom vacancy defects (Fig. 1, B and C); the filled and unfilled symbols are for the simulated armchair (AC) and zigzag (ZZ) tubes, respectively, and the letter labels designate the defect types per Fig. 1. Refer to Eq. 1 in the text. The defect dimensions and the loading direction (indicated by the arrow) are defined in the inset drawing. (**B**) Simulated SWNT relative fracture strength σ_f/σ^* versus the relative defect semilength a/r_0, compared with LEFM prediction for a sharp crack in an infinite-width thin plate (K_{Ic} = 2.69 MPa $m^{0.5}$) and with QFM predictions for sharp ($\rho = 0$, $q = r_0$) and blunt ($\rho = r_0\sqrt{3}/2$, $q = r_0\sqrt{3}$) cracks. Refer to Eqs. 2 and 4 in the text. The far-field stress σ_{ff} and the fracture strength σ_f in these plots are the nominal values at the defect's cross section, adjusted for the infinite-width plate assumption (Materials and Methods). The data are provided in note S4.

(0.8 MPa $m^{0.5}$) and epoxy (0.4 MPa $m^{0.5}$) and comparable to those of nylon (3 MPa $m^{0.5}$) and alumina (4 MPa $m^{0.5}$).

Equation 2 can be rewritten by substituting $K_{Ic} = \sigma^*\sqrt{\pi a^*}$

$$\sigma_f^{LEFM} = \sigma^*\sqrt{\frac{a^*}{a}}, \quad a \geq a^* \tag{3}$$

where $a^* \cong 0.66$ Å is the smallest possible theoretical value for the critical crack semilength (obtained by extrapolating the LEFM line in Fig. 4B). However, a vacancy defect cannot be smaller than a monovacancy, that is, $a_{min} = \frac{3}{4}r_0 \cong 1.07$ Å for an armchair tube or $a_{min} = \frac{\sqrt{3}}{2}r_0 \cong 1.23$ Å for a zigzag tube (note S4), both longer than a^*, and therefore, the region $a < a^*$ is not relevant for vacancy defects. This reasoning resolves the deficiency of LEFM at infinitesimal crack lengths (when $a \to 0$, $\sigma_f \to \infty$) and may be applicable to the fracture of other brittle crystalline nanostructures. In the case of topological defects such as Stone-Wales, lengths shorter than a^* are possible, but the strength of such defective SWNTs is dominated by prestresses, as noted above.

According to LEFM, a brittle crack will propagate spontaneously under stress (that is, become unstable) when the elastic energy released by the structure as a result of crack growth is larger than the energy required to create new crack surfaces. The unstrained region around the crack, approximated in LEFM by a circular shape, is indeed observed by the simulation (the green region in Fig. 3, B and C). The simulated strain energy released by the whole tube when a single carbon-carbon bond is removed is about 22 eV, and grows larger as the crack advances, whereas the energy required to break a single bond is about an order of magnitude lower (*13*, *14*, *35*, *36*). Thus, the energetic condition for crack instability is satisfied.

Quantum fracture mechanics is inconsistent with the simulation of small defects

The simulation is also compared with quantum fracture mechanics (QFM) (*37*), using the theoretical expression for a blunt-tip brittle crack (green dashed lines in Fig. 4B)

$$\sigma_f^{QFM} = K_{Ic}\sqrt{\frac{1 + \rho/2q}{\pi(a + q/2)}} = \sigma^*\sqrt{\frac{1 + \rho/2q}{1 + 2a/q}} \tag{4}$$

where q is the fracture quantum length of atomic scale and ρ is the crack tip radius. This model converges to the classic LEFM brittle model (Eq. 2) for long sharp cracks ($a >> q$, $\rho \to 0$) and to the finite defect-free strength σ^* for an infinitesimal crack ($a/q \to 0$, $\rho/q \to 0$).

Two QFM cases are presented in Fig. 4B, using parametric values suggested by Pugno and Ruoff (*37*): a sharp crack ($\rho = 0$) with $q = r_0$ and a blunt crack ($\rho = q/2$) with $q = \sqrt{3}r_0$. As seen in Fig. 4B, in both cases, the QFM model does not fit the simulation well. The sharp crack fits only the longer defects, while underestimating the strength of the shorter ones, and the blunt crack overestimates the strength of the longer defects. Furthermore, the hypothetical construct of a quantum length q introduced by QFM is not needed for vacancy defects, because the size of a vacancy is never infinitesimal, as shown before, and the defect semilength a is not quantized but can rather vary continuously with rotation of the chirality as illustrated in Fig. 5A. By contrast, the classic LEFM law for a brittle fracture in the presence of a sharp crack (Eq. 2) shows excellent robustness even for defect lengths shorter than a cell size ($a < r_0$).

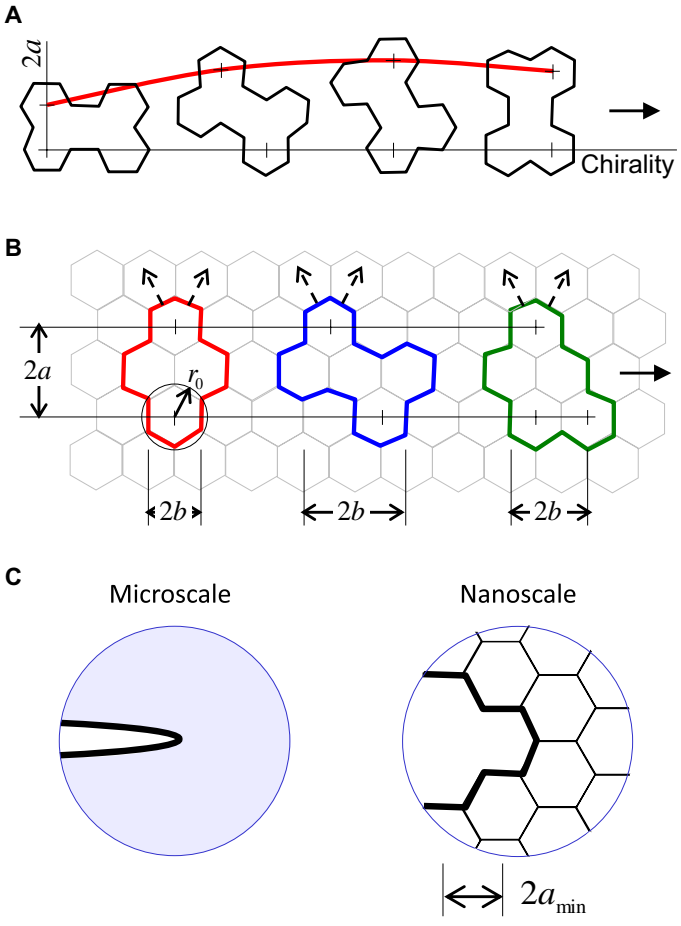

Fig. 5. Defect orientation, shape, and scale. (**A**) Effect of chirality on the defect orientation and length 2*a*. The direction of the load is indicated by the solid arrow. (**B**) Vacancy defects of equivalent SWNT strength, sharing the same length 2*a* and tip curvature r_0, but with different width 2*b*, shape, and orientation. The dashed arrows indicate possible crack propagation paths. (**C**) Comparison of defects at the microscale and nanoscale. Microscale defects are surrounded by a continuum and, if sharp, can cause infinite stress concentrations. Nanoscale defects (that is, SWNT vacancies) are surrounded by a truss-like lattice (they are not sharp), cause finite stress concentrations, and cannot be smaller than a minimal size $2a_{min}$ (the length of a monovacancy).

The simulation results (Fig. 4B) show that the most harm is done by defects of length up to about twice a cell size ($a \approx 2r_0$), with reduced strength down to about 40% of the defect-free strength. Extrapolation to longer defects shows that the strength becomes less sensitive to further increase in defect size. Furthermore, the simulation shows that the crack shape, width, and curvature have only a mild influence on the fracture toughness, as seen in Fig. 4B by the fairly narrow dispersion of the strength values with respect to the LEFM prediction. For example, the number of missing atoms in a defect is not significant, except when they are aligned in such a way that *a* is increased (for example, the three-atom vacancies in Fig. 4B).

Stress concentration and fracture toughness are interrelated

It is evident from these observations that the behavior of the stress concentration and fracture toughness in SWNTs with vacancy defects is not similar to that of a thin plate with elliptical or rounded-tip holes. An SWNT is fundamentally different in structure compared with a thin plate, in that it is basically a truss consisting of members (that is, bonds) with stiffness that is dominant along the bond axis but with flexible angular joints at the atom sites. Compared with a continuum solid, such a structure can more effectively diffuse a local high stress over a large region around the defect, leading to lower stress concentrations. See the illustration in Fig. 5C.

Although the simulation fits the LEFM theory for sharp brittle cracks, the stress at the defect tip is not infinite, as predicted by elastic theory. This seeming contradiction can be resolved by observing that a defect at the nanoscale is not sharp and has a minimal size (Fig. 5C). Similarly, we have shown that the critical condition for crack propagation can be derived both from free energy (fracture mechanics) and from stress concentration considerations. Consequently, we can formulate a simple relationship between the stress concentration and fracture toughness. Because the behavior of an SWNT under tension is almost perfectly linearly elastic (Fig. 2A), and, as shown, the stress concentration remains almost constant with the strain, one can write the stress concentration in the following form

$$K_t = \frac{\sigma_{max}}{\sigma_{ff}} \cong \frac{\sigma^*}{\sigma_f} \quad (5)$$

In words, a gradual increase in the far-field stress σ_{ff} up to the CNT fracture strength σ_f causes a linear rise (with slope K_t) in the stress at the defect tip σ_{max} up to the ideal CNT strength σ^* (equivalent to the bond failure strength, as discussed in note S2).

Substituting σ_f from Eq. 2 into Eq. 5, we obtain

$$K_t \cong \frac{\sigma^*}{K_{Ic}}\sqrt{\pi a} \quad (6)$$

This equation is in agreement with the power fit $K_t \cong 1.5(a/r_0)^{0.5}$ to the stress concentration simulation data (Fig. 4A), where the prefactor is $(\sigma^*/K_{Ic})\sqrt{\pi r_0} \cong 1.5$. Hence, for a given defect of semilength *a*, the stress concentration factor, essentially a geometric property at the macroscale, can be obtained from the SWNT material properties—the fracture toughness K_{Ic} and ideal strength σ^*. This result is not obtainable for a sharp crack in a continuum solid, because σ_{max} in Eq. 5 would diverge. An equivalent form to Eq. 6 can be written by rearranging Eq. 3

$$K_t \cong \sqrt{\frac{a}{a^*}}, \quad a \geq a^* \quad (7)$$

We have shown that both the stress concentration and fracture strength depend predominantly on the defect's length, whereas its shape, width, and orientation are irrelevant. Because the SWNT structure consists of a repeating fixed-size ring-shaped hexagonal cell, the highly stressed defect tip has the same shape and size in all vacancy defects. The tip can be rotated at various angles with respect to the tube main axis, as shown in Fig. 5A, but its shape remains unchanged. Thus, the common hexagonal tip shape seems to cause a similar effect on different defect shapes and orientations. For example, according to the simulation, the three defects in Fig. 5B can be regarded as equivalent in strength and toughness because they have the same length perpendicular to the tube axis, even though their shape, width, and orientation are very different. Even when the defect edge consists of a pair of adjacent hexagonal cells (for example, in the rightmost shape in Fig. 5A and in the bottom edge of the rightmost shape in Fig. 5B),

the stress concentration is localized at each individual cell, with a seemingly negligible effect on its neighbor, and therefore, the tip curvature remains effectively that of a single cell. By analogy, different microscale defects having the same tip curvature are often estimated as having equivalent stress concentrations by fitting an equivalent ellipse to the defect tip (*29*).

DISCUSSION

Stress concentration, arising at a defect tip in an SWNT under tension at room temperature, leads to initiation of a crack that propagates relentlessly until failure. Fracturing occurs at strains as low as 7% and is brittle rather than plastic. Common types of defects, particularly vacancy defects with two to three missing atoms, can degrade the ideal strength of SWNTs by up to about 60%. Reduction in the number of defects during SWNT growth, purification, chemical treatment, and application is therefore an important objective.

Defects at the nanoscale are not sharp, and consequently, stress concentrations are finite and moderated by the SWNT's truss-like structure. The simulated SWNT fracture toughness is 2.7 MPa $m^{0.5}$, which is of the same order as recently reported for graphene (*33*) and typical of moderately brittle materials, somewhat surprising in view of the high elastic flexibility of SWNTs compared to other brittle materials. The simulated strength conforms nicely with the classic theory of LEFM, even for the smallest possible vacancy defect (that is, a monovacancy). The defect length orthogonal to the loading direction and its hexagonal tip shape (common to all vacancies) are the dominant parameters.

The proposed approach and simulation method can be expanded to investigating the brittle fracturing of other carbon nanomaterials containing defects, such as graphene, multiwalled nanotubes (MWNTs), and fullerenes, as well as inorganic nanotubes such as tungsten disulfide (WS_2NT). On the basis of the current study, we expect that graphene should be as susceptible to vacancy defects as an SWNT, with a crack propagation similarly driven by stress concentration. Because the tensile strains induced by rolling a graphene monolayer into an SWNT are negligible (note S3), our results—including the calculated fracture toughness—are directly applicable to graphene. By contrast, we expect that MWNTs and WS_2NTs will be less susceptible to vacancy defects, because crack propagation may be partially inhibited between adjacent layers. At the larger scale of nanocomposite structures (*38*–*45*), further inhibition of crack propagation is expected, particularly when the CNTs are compactly arranged in aligned conformations such as CNT fibers (*46*) or CNT forests (*47*).

MATERIALS AND METHODS

SWNTs and tensile loading

Two SWNT configurations, which represent the two extreme chiralities of an SWNT, were selected for the simulation: an armchair tube with chirality (10, 10) and a zigzag tube with chirality (17, 0). We used SWNTs with an external diameter of 13.56 Å (armchair) and 13.31 Å (zigzag) and with a length of 170 Å in both cases (Fig. 1A). The defects are located approximately at the center of the tubes. A fixed boundary was imposed in a small region (less than 3 Å in length) at one end of the SWNT. At the opposite end, tensile load was simulated by applying a constant displacement rate of 0.001 Å/fs to the atoms. The simulated tensile loading is quasi-static, using adequately small time steps.

Defect types

Both SWNT chiralities allow insertion of a wide variety of vacancies and Stone-Wales defects, with their vertices pointing orthogonally to the tube axis (armchair tube) or along the tube axis (zigzag tube). If desired, each defect type can be oriented at any angle with respect to the tube main axis, given a tube chirality in between armchair and zigzag. The simulated defects are shown in Fig. 1B (armchair tube) and Fig. 1C (zigzag tube) and are designated (a) for Stone-Wales and (b to i) for vacancies. A Stone-Wales defect was simulated by a ~90° rotation of a carbon-carbon bond, which produced two pentagons and two heptagons coupled in pairs (5-7-7-5) (*15*). This defect is stable and may appear spontaneously at very high strains (>20%) when the defect's formation energy barrier is low. A vacancy defect was simulated by removing one or more atoms from their regular atomic sites in the crystalline structure (*12*). This defect is metastable at room temperature for macroscopic times (*12*). Vacancy defects up to three missing atoms were studied, as such small defects are predominant (*12*, *13*, *15*).

Simulation tools

The simulation was executed using the LAMMPS (large-scale atomic/molecular massively parallel simulator) MD simulator (*48*) with the COMPASS force field (*49*). This force field is widely used and validated and has the necessary precision for simulating the variations in potential arising from small elastic deformations, enabling accurate prediction of the CNT structural deformation. The simulation results are practically deterministic, without observable statistical dispersion. The simulation was conducted in an NVT (conservation of substance, volume, and temperature) ensemble at 20°C. For the purpose of stress calculation, the thickness of the SWNT wall was taken as 0.34 nm, which is the equilibrium spacing between two graphite layers (*50*, *51*). A maximum allowed bond force of 10 nN, derived from the bond dissociation energy (*28*), was used to determine whether the bond strength was exceeded (*27*). This criterion enables detection of the crack initiation and tracing of the crack propagation, as well as evaluation of the criticality of different types of defects. See more details in notes S1 and S2.

Infinite-width plate approximation

The underlying assumption is that the SWNT can be unfolded to a thin plate of width πD (D is the tube diameter), which can be regarded as an infinite-width plate with respect to the defect length. Because the ratio between the defect length and the tube perimeter, $\alpha = 2a/\pi D$, is not negligible (ranging from 0.05 to 0.15 for the studied vacancy defects), the far-field stress σ_{ff} and the strength σ_f in Fig. 4 were divided by $1 - \alpha$ to obtain nominal values at the defect's cross section. In this way, the simulation results are adjusted for an infinite-width plate, making them comparable with the used theoretical models from solid mechanics.

Edge effects in finite-width plate models are shown to be negligible. The accuracy of the stress concentration factor in the presence of an elliptical hole in an infinite-width plate with respect to a finite-width plate is better than 2%, estimated by substituting the ratio α into the expression for a finite-width plate (*52*)

$$K_t^{LE} \cong \sum_{i=1}^{4} c_i \left(a/b\right) \alpha^{i-1} \quad (8)$$

The coefficients $c_i(a/b)$ are functions of the ratio a/b, specific for each of the studied defects. Similarly, the accuracy of the fracture strength in the presence of a sharp crack in an infinite-width plate with respect to a finite-width plate is better than 1%, estimated by substituting the ratio α into the expression for a finite-width plate (*53*)

$$\sigma_f^{LEFM} = \frac{K_{Ic}}{\sqrt{\pi a}} \left(\frac{\sqrt{1-\alpha}}{1 - 0.5\alpha + 0.326\alpha^2} \right) \quad (9)$$

SUPPLEMENTARY MATERIALS

Supplementary material for this article is available at http://advances.sciencemag.org/cgi/content/full/2/2/e1500969/DC1

Note S1. Molecular dynamics.
Note S2. Bond failure criterion.
Note S3. Defect-free SWNT under tension.
Note S4. SWNT with defects under tension.
Note S5. Effect of prestresses in topological defects.
Note S6. Comparison with solid mechanics theories.
Note S7. Alternative estimation of the SWNT fracture toughness.
Table S1. Defect dimensions and simulation results.
Fig. S1. Simulated stresses around a Stone-Wales defect.
Movie S1. Crack propagation illustration (separate file).
References (*54*–*61*)

REFERENCES AND NOTES

1. E. W. Wong, P. E. Sheehan, C. M. Lieber, Nanobeam mechanics: Elasticity, strength, and toughness of nanorods and nanotubes. *Science* **277**, 1971–1975 (1997).
2. M. B. Nardelli, B. I. Yakobson, J. Bernholc, Brittle and ductile behavior in carbon nanotubes. *Phys. Rev. Lett.* **81**, 4656–4659 (1998).
3. B. G. Demczyk, Y. M. Wanga, J. Cumingsa, M. Hetmana, W. Hana, A. Zettla, R. O. Ritchie, Direct mechanical measurement of the tensile strength and elastic modulus of multiwalled carbon nanotubes. *Mater. Sci. Eng. A* **334**, 173–178 (2002).
4. M. B. Nardelli, B. I. Yakobson, J. Bernholc, Mechanism of strain release in carbon nanotubes. *Phys. Rev. B* **57**, R4277–R4280 (1998).
5. Q. Zhao, M. B. Nardelli, J. Bernholc, Ultimate strength of carbon nanotubes: A theoretical study. *Phys. Rev. B* **65**, 144105 (2002).
6. T. Dumitrica, M. Hua, B. I. Yakobson, Symmetry-, time-, and temperature-dependent strength of carbon nanotubes. *Proc. Natl. Acad. Sci. U.S.A.* **103**, 6105–6109 (2006).
7. M.-F. Yu, O. Lourie, M. J. Dyer, K. Moloni, T. F. Kelly, R. S. Ruoff, Strength and breaking mechanism of multiwalled carbon nanotubes under tensile load. *Science* **287**, 637–640 (2000).
8. A. H. Barber, I. Kaplan-Ashiri, S. R. Cohen, R. Tenne, H. D. Wagner, Stochastic strength of nanotubes: An appraisal of available data. *Compos. Sci. Technol.* **65**, 2380–2384 (2005).
9. A. H. Barber, R. Andrews, L. S. Schadler, H. D. Wagner, On the tensile strength distribution of multiwalled carbon nanotubes. *Appl. Phys. Lett.* **87**, 203106 (2005).
10. A. H. Barber, S. R. Cohen, A. Eitan, L. S. Schadler, H. D. Wagner, Fracture transitions at a carbon-nanotube/polymer interface. *Adv. Mater.* **18**, 83–87 (2006).
11. B. Peng, M. Locascio, P. Zapol, S. Li, S. L. Mielke, G. C. Schatz, H. D. Espinosa, Measurements of near-ultimate strength for multiwalled carbon nanotubes and irradiation-induced cross-linking improvements. *Nat. Nanotechnol.* **3**, 626–631 (2008).
12. M. Sammalkorpi, A. Krasheninnikov, A. Kuronen, K. Nordlund, K. Kaski, Mechanical properties of carbon nanotubes with vacancies and related defects. *Phys. Rev. B* **70**, 245416 (2004).
13. S. L. Zhang, S. L. Mielke, R. Khare, D. Troya, R. S. Ruoff, G. C. Schatz, T. Belytschko, Mechanics of defects in carbon nanotubes: Atomistic and multiscale simulations. *Phys. Rev. B* **71**, 115403 (2005).
14. S. Zhang, T. Zhu, T. Belytschko, Atomistic and multiscale analyses of brittle fracture in crystal lattices. *Phys. Rev. B* **76**, 094114 (2007).
15. M. Kabir, S. Mukherjee, T. Saha-Dasgupta, Substantial reduction of Stone-Wales activation barrier in fullerene. *Phys. Rev. B* **84**, 205404 (2011).
16. B. I. Yakobson, M. P. Campbell, C. J. Brabec, J. Bernholc, High strain rate fracture and C-chain unraveling in carbon nanotubes. *Comput. Mater. Sci.* **8**, 341–348 (1997).
17. L. G. Zhou, S. Q. Shi, Molecular dynamic simulations on tensile mechanical properties of single-walled carbon nanotubes with and without hydrogen storage. *Comput. Mater. Sci.* **23**, 166–174 (2002).
18. K. Mylvaganam, L. C. Zhang, Important issues in a molecular dynamics simulation for characterising the mechanical properties of carbon nanotubes. *Carbon* **42**, 2025–2032 (2004).
19. K. M. Liew, X. Q. He, C. H. Wong, On the study of elastic and plastic properties of multi-walled carbon nanotubes under axial tension using molecular dynamics simulation. *Acta Mater.* **52**, 2521–2527 (2004).
20. T. Ragab, C. Basaran, A framework for stress computation in single-walled carbon nanotubes under uniaxial tension. *Comput. Mater. Sci.* **46**, 1135–1143 (2009).
21. C. F. Cornwell, C. R. Welch, Very-high-strength (60-GPa) carbon nanotube fiber design based on molecular dynamics simulations. *J. Chem. Phys.* **134**, 204708 (2011).
22. H. D. Wagner, O. Lourie, Y. Feldman, R. Tenne, Stress-induced fragmentation of multiwall carbon nanotubes in a polymer matrix. *Appl. Phys. Lett.* **72**, 188–190 (1998).
23. Z. Xia, W. A Curtina, H. Lia, B. W. Sheldona, J. Lianga, B. Changa, J. M. Xu, Direct observation of toughening mechanisms in carbon nanotube ceramic matrix composites. *Acta Mater.* **52**, 931–944 (2004).
24. G. L. Hwang, Y.-T. Shieh, K. C. Hwang, Efficient load transfer to polymer-grafted multi-walled carbon nanotubes in polymer composites. *Adv. Funct. Mater.* **14**, 487–491 (2004).
25. K. Li, G. Eres, J. Howe, Y.-J. Chuang, X. Li, Z. Gu, L. Zhang, S. Xie, Z. Pan, Self-assembly of graphene on carbon nanotube surfaces. *Sci. Rep.* **3**, 2353 (2013).
26. M. Estili, Y. Sakka, A. Kawasaki, Unprecedented simultaneous enhancement in strain tolerance, toughness and strength of Al_2O_3 ceramic by multiwall-type failure of a high loading of carbon nanotubes. *Nanotechnology* **24**, 155702 (2013).
27. D. M. Heyes, Pressure tensor of partial-charge and point-dipole lattices with bulk and surface geometries. *Phys. Rev. B* **49**, 755–764 (1994).
28. J. J. Vilatela, A. H. Windle, Yarn-like carbon nanotube fibers. *Adv. Mater.* **22**, 4959–4963 (2010).
29. W. D. Pilkey, D. F. Pilkey, *Peterson's Stress Concentration Factors* (Wiley, Hoboken, NJ, ed. 3, 2008), 560 pp.
30. A. A. Griffith, The phenomena of rupture and flow in solids. *Philos. Trans. R. Soc. London Ser. A* **221**, 582–593 (1921).
31. G. R. Irwin, Analysis of stresses and strains near the end of a crack traversing a plate. *J. Appl. Mech.* **24**, 361–364 (1957).
32. H. L. Ewalds, R. J. H. Wanhill, *Fracture Mechanics* (Edward Arnold, London, ed. 2, 1984), 304 pp.
33. Z. Zhang, A. Kutana, B. I. Yakobson, Edge reconstruction-mediated graphene fracture. *Nanoscale* **7**, 2716–2722 (2015).
34. F. Ashby, D. R. H. Jones, *Engineering Materials 1: An Introduction to Properties, Applications and Design* (Butterworth-Heinemann, Oxford, 2011), 496 pp.
35. O. M. Yaghi, Q. Li, Reticular chemistry and metal-organic frameworks for clean energy. *MRS Bull.* **34**, 682–690 (2009).
36. P. G. Collins, in *Oxford Handbook of Nanoscience and Technology: Frontiers and Advances,* A. V. Narlikar, Y. Y. Fu, Eds. (Oxford Univ. Press, Oxford, 2009).
37. N. M. Pugno, R. S. Ruoff, Quantized fracture mechanics. *Philos. Mag.* **84**, 2829–2845 (2004).
38. E. T. Thostenson, T.-W. Chou, Aligned multi-walled carbon nanotube-reinforced composites: Processing and mechanical characterization. *J. Phys. D.* **35**, L77–L80 (2002).
39. Y.-L. Li, I. A. Kinloch, A. H. Windle, Direct spinning of carbon nanotube fibers from chemical vapor deposition synthesis. *Science* **304**, 276–278 (2004).
40. V. P. Veedu, A. Cao, X. Li, K. Ma, C. Soldano, S. Kar, P. M. Ajayan, M. N. Ghasemi-Nejhad, Multifunctional composites using reinforced laminae with carbon-nanotube forests. *Nat. Mater.* **5**, 457–462 (2006).
41. M. Moniruzzaman, J. Chattopadhyay, W. E. Billups, K. I. Winey, Tuning the mechanical properties of SWNT/nylon 6,10 composites with flexible spacers at the interface. *Nano Lett.* **7**, 1178–1185 (2007).
42. J. J. Vilatela, L. Deng, I. A. Kinloch, R. J. Young, A. H. Windle, Structure of and stress transfer in fibres spun from carbon nanotubes produced by chemical vapour deposition. *Carbon* **49**, 4149–4158 (2011).
43. S. Ryu, Y. Lee, J.-W. Hwang, S. Hong, C. Kim, T. G. Park, H. Lee, S. H. Hong, High-strength carbon nanotube fibers fabricated by infiltration and curing of mussel-inspired catecholamine polymer. *Adv. Mater.* **23**, 1971–1975 (2011).
44. J. Qiu, J. Terrones, J. J. Vilatela, M. E. Vickers, J. A. Elliott, A. H. Windle, Liquid infiltration into carbon nanotube fibers: Effect on structure and electrical properties. *ACS Nano* **7**, 8412–8422 (2013).
45. I. Greenfeld, H. D. Wagner, Nanocomposite toughness, strength and stiffness: Role of filler geometry. *Nanocomposites* **1**, 3–17 (2015).
46. M. Zu, Q. Li, Y. Zhu, M. Dey, G. Wang, W. Lu, J. M. Deitzel, J. W. Gillespie Jr., J.-H. Byun, T.-W. Chou, The effective interfacial shear strength of carbon nanotube fibers in an epoxy matrix characterized by a microdroplet test. *Carbon* **50**, 1271–1279 (2012).
47. E. J. Garcia, B. L. Wardle, A. J. Hart, Joining prepreg composite interfaces with aligned carbon nanotubes. *Compos. Part A* **39**, 1065–1070 (2008).
48. C. Ringl, H. M. Urbassek, A LAMMPS implementation of granular mechanics: Inclusion of adhesive and microscopic friction forces. *Comput. Phys. Commun.* **183**, 986–992 (2012).

49. H. Sun, COMPASS: An ab initio force-field optimized for condensed-phase applications—Overview with details on alkane and benzene compounds. *J. Phys. Chem. B.* **102**, 7338–7364 (1998).
50. L. Yang, L. Tong, X. He, MD simulation of carbon nanotube pullout behavior and its use in determining mode I delamination toughness. *Comput. Mater. Sci.* **55**, 356–364 (2012).
51. L. Yang, L. Tong, X. He, H. D. Wagner, R. Wang, Molecular dynamic simulation of oblique pullout of carbon nanotube from resin. *Comput. Mater. Sci.* **83**, 504–512 (2014).
52. W. C. Young, R. G. Budynas, *Roark's Formulas for Stress and Strain* (McGraw-Hill, New York, ed. 7, 2002), 736 pp.
53. D. P. Rooke, D. J. Cartwright, *Compendium of Stress Intensity Factors* (HMSO Ministry of Defence, Procurement Executive, London, 1976), 330 pp.
54. L. V. Zhigilei, A. N. Volkov, A. M. Dongare, in *Encyclopedia of Nanotechnology*, B. Bhushan, Ed. (Springer, Heidelberg, 2012), pp. 470–480.
55. J. Hu, X. Ruan, Y. P. Chen, Thermal conductivity and thermal rectification in graphene nanoribbons: A molecular dynamics study. *Nano Lett.* **9**, 2730–2735 (2009).
56. N. Yang, G. Zhang, B. Li, Thermal rectification in asymmetric graphene ribbons. *Appl. Phys. Lett.* **95**, 033107 (2009).
57. W.-R. Zhong, M.-P. Zhang, B.-Q. Ai, D.-Q. Zheng, Chirality and thickness-dependent thermal conductivity of few-layer graphene: A molecular dynamics study. *Appl. Phys. Lett.* **98**, 113107 (2011).
58. J. W. Zhang, X. He, L. Yang, G. Wu, J. Sha, C. Hou, C. Yin, A. Pan, Z. Li, Y. Liu, Effect of tensile strain on thermal conductivity in monolayer graphene nanoribbons: A molecular dynamics study. *Sensors* **13**, 9388–9395 (2013).
59. M. Murat, M. Anholt, H. D. Wagner, Fracture-behavior of short-fiber reinforced materials. *J. Mater. Res.* **7**, 3120–3131 (1992).
60. G. López-Polín, C. Gómez-Navarro, V. Parente, F. Guinea, M. I. Katsnelson, F. Pérez-Murano, J. Gómez-Herrero, Increasing the elastic modulus of graphene by controlled defect creation. *Nat. Phys.* **11**, 26–31 (2015).
61. D. Broek, *Elementary Engineering Fracture Mechanics* (Springer Science & Business Media, Dordrecht, ed. 4, 1982), 540 pp.

Acknowledgments: H.D.W. is the recipient of the Livio Norzi Professorial Chair at the Weizmann Institute. L.Y. is indebted to X. He from the Harbin Institute of Technology for his support and guidance. **Funding:** This research was made possible in part by the generosity of the Harold Perlman family. Support from the Israel National Nanotechnology Initiative–Focal Technology Areas Fund is gratefully acknowledged. **Author contributions:** L.Y. initiated the study and ran the MD simulations. I.G. and H.D.W. performed the theoretical analysis, interpreted the results, coordinated the study, and wrote and edited the manuscript. All authors discussed the results and theoretical interpretations. **Competing interests:** The authors declare that they have no competing interests. **Data and materials availability:** All data needed to evaluate the conclusions in the paper are present in the paper and/or the Supplementary Materials. Additional data related to this paper may be requested from I.G. and H.D.W.

Submitted 21 July 2015
Accepted 2 December 2015
Published 5 February 2016
10.1126/sciadv.1500969

Citation: L. Yang, I. Greenfeld, H. D. Wagner, Toughness of carbon nanotubes conforms to classic fracture mechanics. *Sci. Adv.* **2**, e1500969 (2016).

Toughness of carbon nanotubes conforms to classic fracture mechanics

Lin Yang, Israel Greenfeld and H. Daniel Wagner

Sci Adv **2** (2), e1500969.
DOI: 10.1126/sciadv.1500969